Predicted pressure-induced *s-d* electron transition of hydrogen in electride $(Na_2He)_4H$

Yan Gao,[1] Tian Cui,[2,*] and Da Li[1,†]

[1]*State Key Lab of Superhard Materials and Key Laboratory of Material Simulation Methods & Software of Ministry of Education, College of Physics, Jilin University, Changchun 130012, People's Republic of China*

[2]*School of Physical Science and Technology, Ningbo University, Ningbo 315211, People's Republic of China*

(Received 5 November 2023; revised 12 April 2024; accepted 12 April 2024; published 1 May 2024)

Unexpected pressure-induced *s-d* electron transition had been observed in various *s*-block metals. However, it is noteworthy that no such transition has been reported for hydrogen, a unique element within the *s* block of the periodic table. Here, we propose using a zero-dimensional electride state, similar to a diamond anvil cell, to pressurize hydrogen under high pressure. The *s-d* electron transition of hydrogen was confirmed in our predicted electride $(Na_2He)_4H$ at 200 GPa. The electride-state interstitial quasiatoms arranged themselves in a regular octahedral configuration centered at the hydrogen atom. This arrangement established a highly symmetrical Coulomb repulsion field, further compressing and triggering the central hydrogen atom to undergo an *s-d* transition. Additionally, our results indicate that the hydrogen doping results in the metallization and superconductivity of electride $(Na_2He)_4H$. The electride-state interstitial quasiatoms around hydrogen atoms dominate the superconductivity of $(Na_2He)_4H$. The presence of $(Na_2He)_4H$ provides an example to confirm the promotion effect of the electride state on the superconductivity of electrides.

DOI: 10.1103/PhysRevB.109.184102

I. INTRODUCTION

Pressure-induced *s-d* transition is a special electron transition observed in many *s*-block metals. When these metals are compressed, the valence electrons of *s*-block alkali and alkaline-earth metals like light Li, Na, Mg, Cs, and Ba transfer to the originally unoccupied *d* orbitals [1–10]. This phenomenon is a result of changes in the atomic valence electron configuration and atomic orbital energies brought by high pressure. Interestingly, the *s-d* transition of *s*-block metals often accompanies the formation of high-pressure electrides. Some of the valence electrons of *s*-block alkali and alkaline-earth metal elements easily leave the original *s* orbital and enter the lattice cavities under high pressure. This results in the formation of electride-state interstitial quasiatoms (ISQs), behaving as anions [8]. The presence of electride-state ISQs leads to unexpected physical properties. For instance, alkali lithium undergoes a metal-insulator-metal phase transition accompanying electride-state formation [11,12]. Sodium, under high pressure, can react with chemically inert helium, giving rise to an unexpected electride, Na_2He, featuring isolated spherical electride states [13].

Despite reports of *s-d* transition of most *s*-block metal elements and their intriguing physicochemical properties at high pressure, such a transition has yet to be observed in hydrogen, a unique *s*-block element in the periodic table. The possible energy levels of *d* orbitals of hydrogen were theoretically proposed in an idealized confined hydrogen-atom model. However, a substance with actual *d*-orbital occupation of hydrogen is still missing [14–16]. Small atomic radius of hydrogen gives its nucleus a strong control over its lone valence electron. Achieving *s-d* transition of hydrogen under pure high-pressure conditions is challenging. For example, when two hydrogen atoms come together, they form a highly stable covalent H_2 molecule through *s* orbital–*s* orbital interaction. Similarly, hydrogen forms polar covalent bonds through its *s* orbital when it encounters highly electronegative elements such as F, Cl, and Br, under ambient conditions. Even in complex hydrogen molecular units, electrons typically occupy the ground-state MOs composed of hydrogen *s* orbitals. Within hydrogen-rich hydride superconductors [17,18], a popular topic in condensed matter physics, electrons still fill the lower-energy MOs composed of hydrogen *s* orbitals. Consequently, the Fermi level of a hydrogen-rich hydride superconductor is primarily governed by the *s* electrons of hydrogen. These suggest that the *s-d* transition of hydrogen is an unfeasibly difficult task. However, the presence of electride-state ISQs seems to open opportunities to achieve *s-d* transition of hydrogen because it can provide a purely Coulomb repulsive force, which may have a significant impact on the energy levels of hydrogen orbitals under high pressure. To date, there are no reports of the interaction between electride-state ISQs and hydrogen under high pressure. Furthermore, a real stable compound with a sufficient electride state and hydrogen has yet to be discovered.

Here, with the experimentally synthesized electride Na_2He as an example, we investigated the feasibility of using a high-pressure and electride-state ISQs to achieve *s-d* transition of hydrogen. Several different electrides Na_2HeH_x with *d*-orbital occupation of hydrogen were proposed. Furthermore, we investigated the hydrogen-doping-induced metallization and superconductivity of high-pressure electride Na_2HeH_x,

*Corresponding author: cuitian@nbu.edu.cn
†Corresponding author: dali@jlu.edu.cn

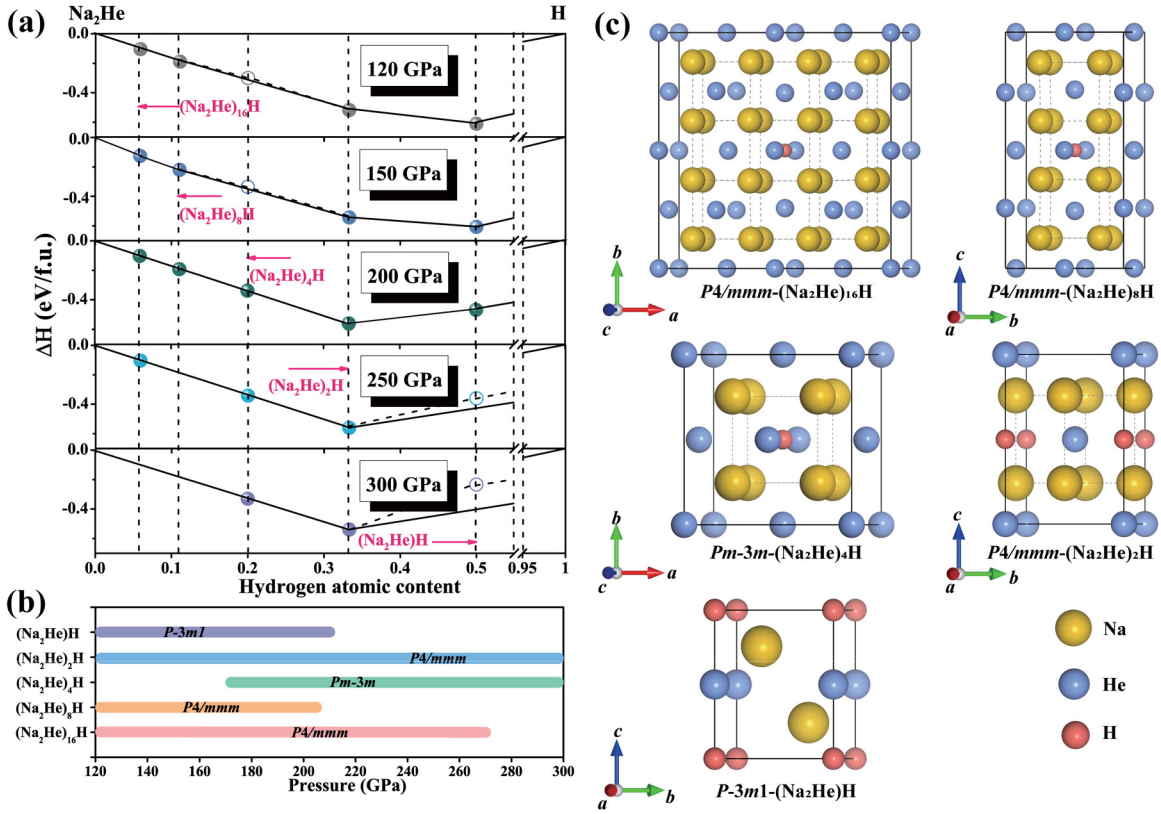

FIG. 1. (a) Convex hull of Na_2HeH_x. Solid and hollow balls correspond to thermodynamically stable and metastable stoichiometries, respectively. (b) Phase transition diagram of five stable compounds. (c) Crystal structures of $P4/mmm$-$(Na_2He)_{16}H$ at 150 GPa, $P4/mmm$-$(Na_2He)_8H$ at 120 GPa, $Fm\bar{3}m$-$(Na_2He)_4H$ at 200 GPa, $P4/mmm$-$(Na_2He)_2H$ at 120 GPa, and P-$3m1$-$(Na_2He)H$ at 120 GPa. Yellow, blue, and pink balls represent Na, He, and H atoms, respectively.

revealing an intriguing interplay between electride-state ISQs and superconductivity.

II. METHOD

To search the thermodynamically stable compounds of the Na_2He-H system, the global structure search was implemented by using the crystal structure analysis via particle swarm optimization (CALYPSO) [19–21] code. CALYPSO structure prediction can determine the low-energy crystalline structures based on the known chemical composition, and the predictions on $(Na_2He)_xH$ ($4 \geqslant x \geqslant 1$) at 120–300 GPa were considered in this work. More detailed parameters about structural predictions are provided in the Supplemental Material [22]. The dynamical stability of several thermodynamically stable Na_2HeH_x compounds was examined using the PHONOPY code [23]. The electronic property calculations were performed in the framework of density functional theory (DFT) [24], as implemented in the Vienna *ab initio* simulation package (VASP) [25]. The generalized gradient-corrected scheme of Perdew-Burke-Ernzerhof was employed [26], and the $3s^1$, $1s^2$, and $1s^1$ configurations were adopted for the valence electrons of Na, He, and H, respectively. The electron-ion interactions were analyzed using the projector-augmented-wave (PAW) method [27], and the plane-wave basis set was constructed by adopting an energy cutoff of 600 eV, which was determined to be sufficiently precise through convergence tests. The Monkhorst-Pack scheme was adopted, and the k-mesh spacing was set as $2\pi \times 0.02\,\text{Å}^{-1}$ [28]. T_cs were calculated via the QUANTUM ESPRESSO package [29]. Ultrasoft potentials with a kinetic energy cutoff of 100 Ry were considered, and $24 \times 24 \times 24$ k points and $6 \times 6 \times 6$ q points were adopted for the electron Brillouin region integration and the evaluation of the phonon mode contribution, respectively. The three-dimensional (3D) Fermi surface was depicted with the Fermi Surfer viewer [30]. The bonding states were obtained based on the crystal orbital Hamilton population (COHP) analysis implemented in LOBSTER [31].

III. RESULTS AND DISCUSSION

A global structure search of the Na_2He-H system throughout the pressure range 120–300 GPa was carried out by using the CALYPSO code combined with first-principles calculations. A convex hull with the zero-point energy correction was reasonably constructed to confirm the thermodynamical stability of Na_2HeH_x by calculating the corresponding formation enthalpy $\Delta H(Na_2HeH_x)$, which was defined as $\Delta H(Na_2HeH_x) = H(Na_2HeH_x) - H(Na_2He) - xH(H)$, where $H(Na_2HeH_x)$, $H(Na_2He)$, and $H(H)$ represent the enthalpies of stable Na_2HeH_x, Na_2He, and H, respectively [Fig. 1(a)]. $Fm\bar{3}m$-Na_2He and $C2/c$-H were adopted as reference structures at the corresponding pressure conditions [13,32,33]. Five thermodynamically stable electrides ($(Na_2He)_{16}H$, $(Na_2He)_8H$, $(Na_2He)_4H$, $(Na_2He)_2H$, and $(Na_2He)H$) were predicted. $(Na_2He)_{16}H$, $(Na_2He)_8H$,

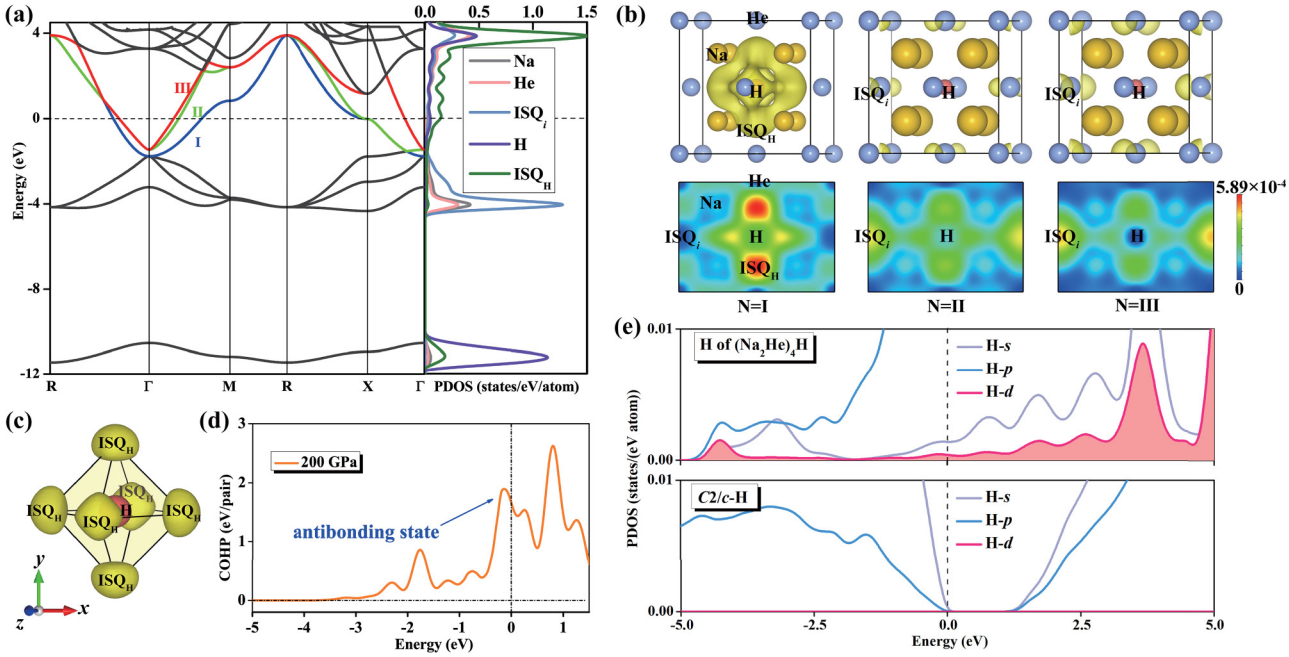

FIG. 2. (a) Band structure and projected density of states (PDOS) of $(Na_2He)_4H$ at 200 GPa. (b) The three-dimensional (3D) and corresponding two-dimensional (2D) band-decomposed charge density distributions for the (110) plane within the energy interval of −0.1 and 0 eV. The left, middle, and right sections correspond to contributions from bands I, II, and III, respectively. The isosurface level is set as 4.22×10^{-4} e Å^{-3} for 3D charge density distributions, and the maximum 2D charge density is 5.89×10^{-4} e Å^{-2}. (c) The schematic diagram of the ISQs located at the six vertices of a regular octahedron centered at the H atom. (d) The COHP of ISQs around H atoms and H pairs. (e) Comparison of the PDOS of H of $Fm\bar{3}m$-$(Na_2He)_4H$ and $C2/c$-H at 200 GPa.

$(Na_2He)_4H$, and $(Na_2He)_2H$ have similar structural features, as shown in Fig. 1(c), and can be viewed as adding one H atom to the center of the electride-state ISQ of well-known $Fm\bar{3}m$-Na_2He [13], where the host lattice configuration $Fm\bar{3}m$-Na_2He is well maintained. Imaginary frequencies are absent in the whole Brillouin zone (BZ) of the five thermodynamically stable structures (Fig. S1 of the Supplemental Material [22]), indicating their dynamical stability. The stable crystal structure parameters are summarized in the Table S1 [22], and the detailed electronic structure properties are provided in Fig. S6 [22].

Next, we select $(Na_2He)_4H$ for further in-depth study due to its preferentially highest symmetry (favorable for a more ideal hydrostatic environment) as an example to investigate the feasibility of using a high-pressure electride-state environment to trigger the *s-d* transition of hydrogen. The global thermodynamic stability of $(Na_2He)_4H$ has been verified by the ternary convex hull of the Na-He-H system as shown in Fig. S3 of the Supplemental Material [7,13,33–39]. The computational details have been provided in the Supplemental Material. $(Na_2He)_4H$ crystallizes in the cubic $Fm\bar{3}m$ space group. One hydrogen atom is located in the center of the simple cubic Na sublattice. Bader charge [40] analysis indicates that due to the higher energy of the 3*s* orbital, the valence electrons of Na atoms leave the 3*s* orbitals, as expected, and most of these valence electrons enter the lattice cavities acting as isolated ISQs (defined as ISQ_i for clarity) (Table S6) or aggregate around the H atom (defined as ISQ_H), providing a perfect spherical and highly symmetrical electride-state environment (Fig. S6).

Compared with that of pristine Na_2He, the electronic structure of $Pm\bar{3}m$-$(Na_2He)_4H$ is altered by hydrogen, resulting in an upward shift of the Fermi level [Fig. 2(a) and Fig. S7 [41]]. $(Na_2He)_4H$ becomes a metal with three bands crossing the Fermi level (denoted as band I, band II, and band III). The highly degenerated bands I and II form a flat band at the *X* point, resulting in a Van Hove singularity near the Fermi level. The projected density of states (PDOS) of $Pm\bar{3}m$-$(Na_2He)_4H$ at the deep energy (approximately –25 eV) and shallow energy (–5 to –1.5 eV) levels mainly originates from He and ISQs, similar to that of Na_2He (Fig. S8). Hydrogen barely interacts with other atoms except ISQs, forming a separate band within the energy interval–10 to –12 eV. Additionally, the DOS near the Fermi level is mainly contributed by the ISQ_H around the H atom and central H atom. The band-decomposed charge density within the –0.1 to 0 eV range intuitively reflects the electron distributions near the Fermi level, and the contribution from band I is dominated around the Fermi level as shown in Fig. 2(b). The corresponding 2D sections in the (110) plane clearly demonstrate that electrons contributed by band I almost fully arise from the ISQ_H and the central H atoms. Meanwhile, the electrons contributed by band II and band III are primarily composed of contributions from ISQ_Hs, H atoms, and ISQ_is, with minor contributions from sodium and helium.

According to the charge density distribution at the Fermi level, it is obvious that the valence electrons escaping from the 3*s* orbitals of Na behave as anionic ISQ_Hs aggregated around H atoms rather than occupying the 1*s* orbitals of H atoms. As exhibited in the schematic diagram in Fig. 2(c), these ISQ_Hs

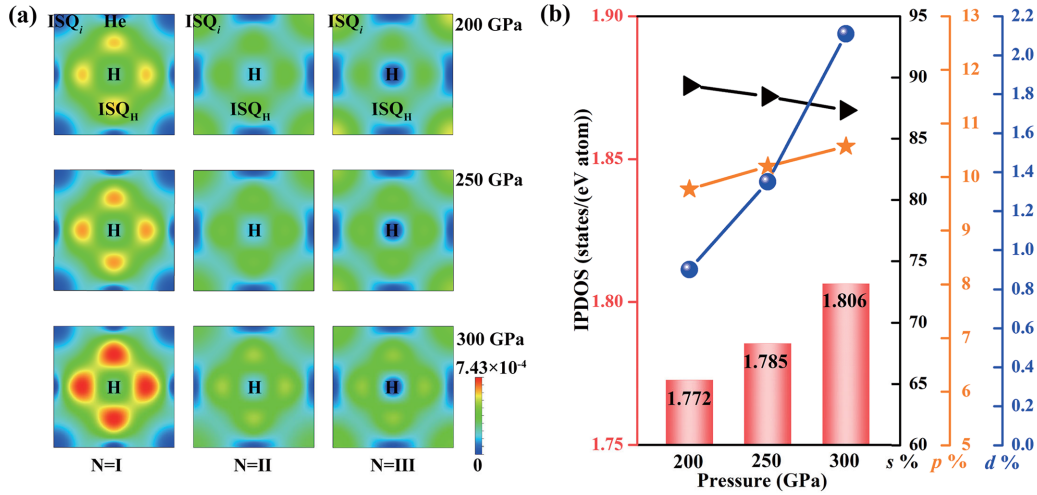

FIG. 3. (a) The 2D band-decomposed charge density distributions of $(Na_2He)_4H$ within the energy interval of –0.1 and 0 eV at various pressures: the left, middle, and right correspond to the contributions from band I, II, and III, respectively. The (100) plane was selected for intuitiveness. The maximum 2D charge density was $7.41 \times 10^{-4}\ e\ Å^{-2}$. (b) The integral projected density of states (IPDOS) of atomic H and the content of each occupied orbital of H at the Fermi level at 200–300 GPa. The IPDOS values of the *s*, *p*, and *d* orbitals at the Fermi level are labeled in black, orange, and blue, respectively.

located at six vertices of a regular octahedron centered at the H atom and three diagonal planes of the regular octahedron are parallel to the *xy*, *yz*, and *zx* planes, respectively, providing a symmetrical Coulomb repulsive field matching the directivity of the four-petal *d* orbital (d_{xy}, d_{yz}, and d_{xz}). As shown in the COHP analysis [Fig. 2(d) and Table S7), the six ISQ_Hs interact with the central hydrogen, and robust antibonding states are generated below the Fermi level. The calculated COHP value at the Fermi level is 1.667 eV/pair, which is much stronger than that of the robust antibonding interaction between Cu 3*d* and I 5*p* (1.25 eV/pair) of $CuBiI_4$ [42]. Such a strong Coulomb repulsive field affects the orbital energy level of H and forces the electrons of the central H atom into the originally unfilled *d* orbital.

To further confirm the *s*-*d* transition of hydrogen, the PDOS of hydrogen is calculated at 200 GPa [Fig. 2(e) and Fig. S9]. The *d* orbitals of hydrogen are remarkably occupied below the Fermi level and contribute to the density of states together with the *s* orbital, while no *d*-orbital occupation was observed in the *C*2/*c*-phase hydrogen under identical compression conditions. Therefore, the electride-state environment shows great potential to modulate the electron orbital occupation of hydrogen. The PDOS of H indicates that the *d* orbitals of hydrogen split into two groups: the occupied triple degenerate T_{2g} (d_{xy}, d_{yz}, and d_{xz}) orbitals and unoccupied double degenerate E_g (d_{z^2} and $d_{x^2-y^2}$) orbitals (Figs. S11 and S12), similar to the energy splitting of the *d* orbitals in an octahedral crystal field [43]. The ISQ_Hs along the vertices of the regular octahedron behave as ligand anions, which produce a strong Coulomb repulsion force on the central H atom. Different from the traditional concept of chemical bonding, these ISQ_Hs only contribute pure compression.

Subsequently, to investigate the effect of Coulomb repulsion on the *s*-*d* transition of hydrogen, the electron density of states of the H atom and ISQ_H under distinct pressure was studied. As shown in Fig. 3(a), the charges of ISQ_Hs aggregated around the H atom become highly localized with a density far higher than that at other positions as the pressure increases. Band I exhibits a considerable contribution to the DOS at the Fermi level. Additionally, the charge density contributed by band II and band III also increases unambiguously under increased compression. Due to the increasing electron density, the Coulomb repulsion interaction between ISQ_Hs and the central H atom at the Fermi level becomes stronger, as quantitatively shown in the COHP results (Fig. S13). The maximum COHPs at the Fermi level are 1.667, 1.853, and 1.998 eV/pair. The forceful Coulomb repulsion field dominates additional parts of the chemical precompression environment, thus increasing the effective pressure even at low external pressures, and the occupied *d* orbitals of hydrogen below the Fermi level move toward deep energy levels (Fig. S14). Moreover, as shown in Fig. 3(b), the IPDOS of hydrogen quantitatively demonstrates that the *d*-orbital and *p*-orbital occupation of hydrogen dramatically increases with increasing pressure, with the contents of the IPDOS of the *d* orbital at the Fermi level increasing from 0.9% to 1.35% and then to 2.11% at 200, 250, and 300 GPa, while the content of the *s* orbital decreases under stronger compression. In conclusion, high pressure and the strong Coulomb repulsion force elevate the *d*-orbital occupation of hydrogen.

Recently, the high-pressure electride superconductors have attracted significant attention. Several notable electride superconductors such as Li_6C, Li_6P, Li_8Au, exhibiting T_c of 10, 39.3, and 73.1 K, respectively, have been predicted [41,44,45]. Despite these advancements, a comprehensive understanding of the superconducting mechanism underlying high-pressure electrides remains elusive. The role of electride-state ISQs in influencing superconductivity is a topic of ongoing debate. Due to the interplay between hydrogen atoms and ISQ_Hs, the insulating Na_2He electride becomes a metal. $(Na_2He)_4H$ becomes an ideal model to investigate the superconductivity of high-pressure electride superconductor.

According to the band structure, a flat band and a steep band near the Fermi level around the *X* and Γ symmetry

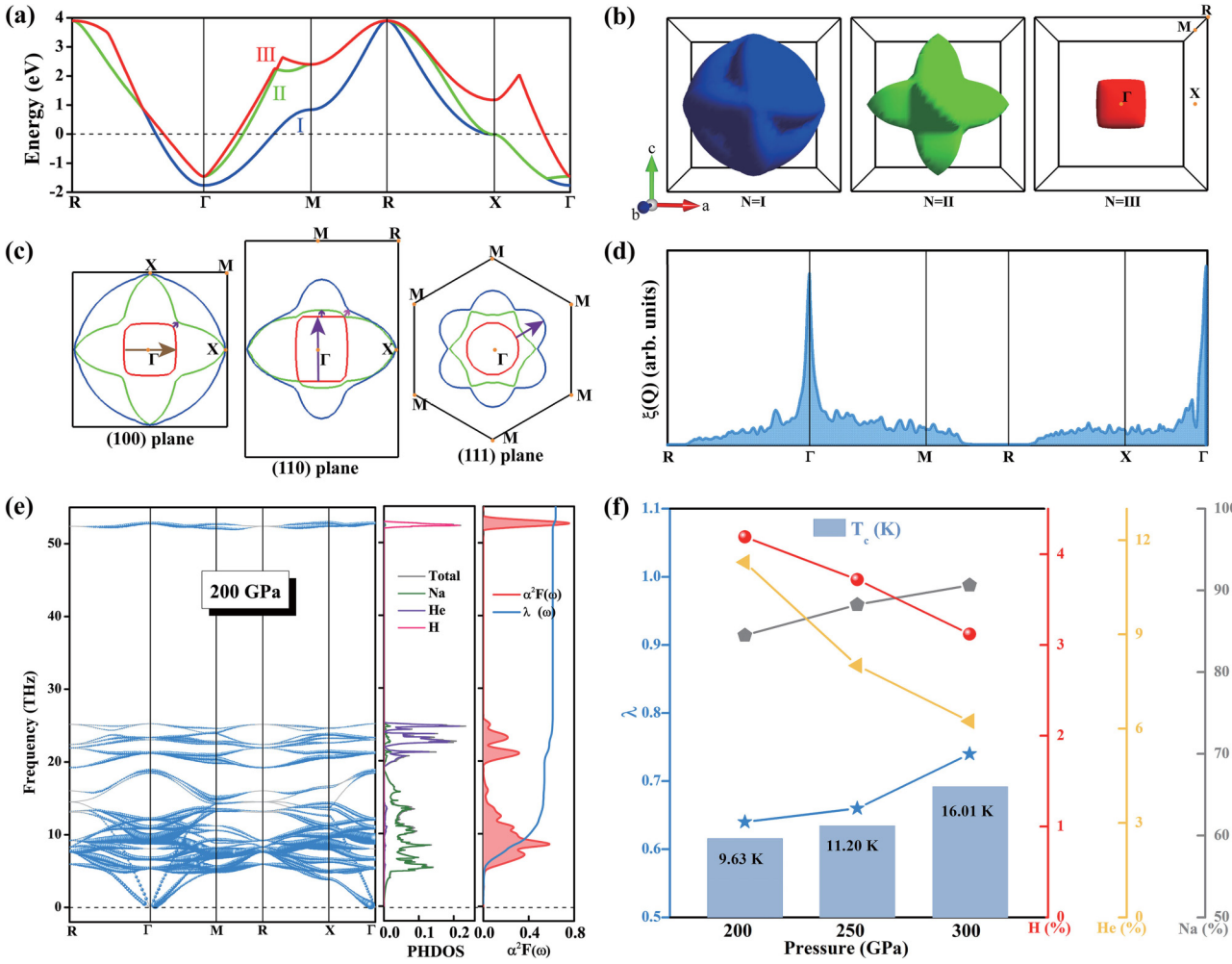

FIG. 4. (a) Electronic band structure of $(Na_2He)_4H$ at 200 GPa. (b) 3D Fermi surface (FS) of bands I, II, and III. (c) 2D plots of FS projected in the (100), (110), and (111) planes. Blue, green, and red lines represent bands I, II, and III, respectively. (d) Nesting function $\xi(q)$ of $(Na_2He)_4H$ at 200 GPa. (e) Calculated phonon dispersion, projected phonon DOS, Eliashberg spectral function $\alpha^2F(\omega)$, and integrated electron-phonon coupling (EPC) parameter $\lambda(\omega)$ of $(Na_2He)_4H$ at 200 GPa. (f) The calculated λ and the contributions of three types of atoms to λ. T_c at various pressures is shown in the columns.

points appear simultaneously, favoring the formation of electron pairing and enhancing superconducting properties [Fig. 4(a)]. The Fermi surface (FS) topology is very important for the superconductivity of a material. The crossing bands develop three electron pockets at the Γ symmetry point, and three Γ-centered closed FS sheets were identified. The FS of the lowest-energy band I forms a blue ball with eight highly symmetric indentations [Fig. 4(b)]. The FS of band II forms a green geometry with six highly symmetric cones. The red roughly cubic structure in the center represents the FS of the highest energy band III. The highly symmetrical Fermi surfaces imply the existence of strong Fermi surface nesting in the BZ, which is beneficial for superconductivity [46]. 2D plots of the FS projected in the (100), (110), and (111) planes are depicted [Fig. 4(c)]. The red cubic FS of band III includes three pairs of opposite faces, resulting in large parallel regions connected by specific phonon wave vectors, which influence the nesting process. They are nearly parallel to the Γ-*X* and Γ-*M* directions in the (100) and (110) planes. The example nesting vectors are shown as brown and purple arrows, respectively. Band II, with an approximate ellipsoidal shape, exhibits a similar parallel face along the Γ-*M* direction in the (110) plane. Additionally, the purple nesting vectors in the (111) and (100) planes indicate the possible nesting vectors along the Γ-*M* direction between band I (II) and band III. In the Γ-*R* direction, the pink nesting vector connects the FSs of band I and band II. At the *X* point, band I and band II have almost coincident FSs, which correspond to the flat band at the *X* point in the energy band structure [Fig. 4(a)].

To give a definitive description of the FS nesting, we calculate the nesting function $\xi(q)$ of $(Na_2He)_4H$ at 200 GPa [Fig. 4(d)] [34,47]. $\xi(q)$ was defined as

$$\xi(q) = \frac{1}{N}\sum_{\vec{k},i,j}\delta(\varepsilon_{\vec{k},i} - \varepsilon_F)\delta(\varepsilon_{\vec{k}+\vec{q},j} - \varepsilon_F),$$

where N corresponds to the number of k points and $\varepsilon_{\vec{k},i}$ and $\varepsilon_{\vec{k}+\vec{q},j}$ are the Kohn-Sham eigenvalues for wave vectors k and $k+q$. i and j are the indexes of the energy bands, and ε_F corresponds to the Fermi energy. The $\xi(q)$ of $(Na_2He)_4H$ has

several sharp peaks in the Γ-*R*, Γ-*M*, and Γ-*X* directions. The strong sharp peak between the Γ and *R* symmetry points (near the Γ point) is related to the FS nesting between band I and band II at the Fermi level. Several sharp peaks between the Γ and *M* symmetry points are attributed to the FS nesting between these three bands. The peaks in the Γ-*X* direction (near the Γ point) originate from the nestings between band I and band II. Fermi surface nesting, especially the nestings around the Γ and *X* points corresponding to the flat and steep bands, contributes to strong electron-phonon interactions, indicating that $(Na_2He)_4H$ approaches electronic instability and acts as a superconductor.

The superconductivity of $(Na_2He)_4H$ at 200 GPa was investigated by using the McMillan-Allen-Dynes formula $T_c = \frac{\omega_{\log}}{1.2}\exp[-\frac{1.04(1+\lambda)}{\lambda-\mu^*(1+0.62\lambda)}]$ where $\omega_{\log}$ represents the logarithmic average of the spectral function and λ and μ^* correspond to the electron-phonon coupling parameter and the typical Coulomb pseudopotential parameter, respectively [48,49]. The T_c of $(Na_2He)_4H$ was determined to be 9.63 K at 200 GPa by using the Eliashberg equation with a typical Coulomb pseudopotential μ^* of 0.13. (The T_cs values with μ^* from 0.1 to 0.13 were calculated, as shown in Table S8.) The calculated EPC parameter λ reaches 0.64 in $(Na_2He)_4H$ at 200 GPa. Due to the difference of atomic mass, the Eliashberg spectral function $\alpha^2F(\omega)$ and projected phonon DOS indicate that λ can be separated into three regions corresponding to the vibration modes of Na, He, and H atoms [Fig. 4(e)]. Na atoms possessing the most substantial atomic mass give a main contribution of 84.5% to the EPC parameter λ below 19 THz at 200 GPa. The lighter He atoms contribute to 11.3% of λ within the frequency interval 19–26 THz at 200 GPa. Only 4.1% of λ is contributed by the lightest hydrogen atom which is related to the high-frequency region (50–60 THz). As discussed previously, most valence electrons of Na atoms transfer into ISQ_Hs. Therefore, unlike that of hydrogen-rich hydride superconductors in which the electrons of hydrogen atoms mainly contribute to the EPC [50], the EPC of $(Na_2He)_4H$ is mainly dominated by the ISQ_Hs around the hydrogen atom instead of hydrogen.

Furthermore, the evolution of T_c with increasing pressure was analyzed. T_c increases to 11.20 K at 250 GPa and reaches 16.01 K at 300 GPa. The T_c evolution of $(Na_2He)_4H$ has a variation trend similar to that of the EPC parameter λ [Fig. 4(f)], indicating that the variation of λ plays a dominant role in the superconductivity. λ_{qv}, which is related to the EPC for the wave vector q with mode v, increases significantly in the *R*-Γ, Γ-*M*, and Γ-*X* directions with increasing pressure (Fig. S15). Remarkably, although the total λ increases with increasing pressure, the contributions of He and H atoms to the total λ decrease with increasing pressure. The detailed evolution of the superconducting properties is summarized in Table S9 [31]. The increase of total λ with increasing pressure can be attributed to the contribution of Na atoms. Therefore, from the electronic structure perspective, the ISQ_Hs around hydrogen are responsible for the increase of total λ with increasing pressure and lead to an increase in the T_c of $(Na_2He)_4H$. The presence of $(Na_2He)_4H$ provides an example to confirm the promotion effect of the electride state on the superconductivity of electrides.

IV. CONCLUSIONS

In summary, we proposed a strategy to achieve the *s-d* transition of hydrogen by using a high-pressure electride-state environment. The *s-d* electron transition of hydrogen was predicted in the electride $(Na_2He)_4H$. The electride-state ISQs around the hydrogen atom form a regular octahedron centered at the hydrogen atom. These ISQs form a highly symmetric Coulomb repulsive force field that forces hydrogen atoms to undergo the *s-d* electron transition. Furthermore, our results indicate that the doping of hydrogen results in the metallization and superconductivity of high-pressure electrides. The electride $(Na_2He)_4H$ displays unexpected superconductivity, with a T_c of 9.63 K at 200 GPa. The electride-state interstitial quasiatoms around hydrogen atoms dominate the superconductivity of $(Na_2He)_4H$. Our results provide a different perspective for understanding the superconductivity of high-pressure electrides.

ACKNOWLEDGMENTS

This work was supported by the National Key R&D Program of China (Grant No. 2023YFA1406200), National Natural Science Foundation of China (Grants No. 12374004 and No. 12174141), and the Graduate Innovation Fund of Jilin University (Grant No. 2023CX034). The calculations were performed at the High Performance Computing Centre of Jilin University, China.

[1] I. Loa, R. J. Nelmes, L. F. Lundegaard, and M. I. McMahon, Extraordinarily complex crystal structure with mesoscopic patterning in barium at high pressure, Nat. Mater. **11**, 627 (2012).

[2] M. Hirayama, R. Okugawa, T. Miyake, and S. Murakami, Topological Dirac nodal lines and surface charges in fcc alkaline earth metals, Nat. Commun. **8**, 14022 (2017).

[3] A. Sanna, C. Franchini, A. Floris, G. Profeta, N. N. Lathiotakis, M. Lüders, M. A. L. Marques, E. K. U. Gross, A. Continenza, and S. Massidda, *Ab initio* prediction of pressure-induced superconductivity in potassium, Phys. Rev. B **73**, 144512 (2006).

[4] J. S. Tse, A chemical perspective on high pressure crystal structures and properties, Natl. Sci. Rev. **7**, 149 (2020).

[5] J. B. Neaton and N. W. Ashcroft, Pairing in dense lithium, Nature (London) **400**, 141 (1999).

[6] I. Tamblyn, J. Raty, and S. A. Bonev, Tetrahedral clustering in molten lithium under pressure, Phys. Rev. Lett. **101**, 075703 (2008).

[7] Y. Ma, M. Eremets, A. R. Oganov, Y. Xie, I. Trojan, S. Medvedev, A. O. Lyakhov, M. Valle, and V. Prakapenka, Transparent dense sodium, Nature (London) **458**, 182 (2009).

[8] M. Miao, Y. Sun, E. Zurek, and H. Lin, Chemistry under high pressure, Nat. Rev. Chem. **4**, 508 (2020).

[9] G. Fabbris, J. Lim, L. S. I. Veiga, D. Haskel, and J. S. Schilling, Electronic and structural ground state of heavy alkali metals at high pressure, Phys. Rev. B **91**, 085111 (2015).

[10] M. I. McMahon, S. Rekhi, and R. J. Nelmes, Pressure dependent incommensuration in Rb-IV, Phys. Rev. Lett. **87**, 055501 (2001).

[11] Y. Yao, S. T. John, and D. D. Klug, Structures of insulating phases of dense lithium, Phys. Rev. Lett. **102**, 115503 (2009).

[12] J. Lv, Y. Wang, L. Zhu, and Y. Ma, Predicted novel high-pressure phases of lithium, Phys. Rev. Lett. **106**, 015503 (2011).

[13] X. Dong, A. R. Oganov, A. F. Goncharov, E. Stavrou, S. Lobanov, G. Saleh, G. Qian, Q. Zhu, C. Gatti, and V. L. Deringer, A stable compound of helium and sodium at high pressure, Nat. Chem. **9**, 440 (2017).

[14] S. Goldman and C. Joslin, Spectroscopic properties of an isotropically compressed hydrogen atom, J. Phys. Chem. **96**, 6021 (1992).

[15] J. L. Marin and S. A. Cruz, Enclosed quantum systems: Use of the direct variational method, J. Phys. B: At. Mol. Opt. Phys. **24**, 2899 (1991).

[16] Y. P. Varshni, Accurate wavefunctions for the confined hydrogen atom at high pressures, J. Phys. B: At. Mol. Opt. Phys. **30**, L589 (1997).

[17] H. Wang, J. S. Tse, K. Tanaka, T. Iitaka, and Y. Ma, Superconductive sodalite-like clathrate calcium hydride at high pressures, Proc. Natl. Acad. Sci. USA **109**, 6463 (2012).

[18] A. P. Drozdov, M. I. Eremets, I. A. Troyan, V. Ksenofontov, and S. I. Shylin, Conventional superconductivity at 203 kelvin at high pressures in the sulfur hydride system, Nature (London) **525**, 73 (2015).

[19] Y. Liu, R. Wang, Z. Wang, D. Li, and T. Cui, Formation of twelve-fold iodine coordination at high pressure, Nat. Commun. **13**, 412 (2022).

[20] Y. Wang, J. Lv, L. Zhu, and Y. Ma, CALYPSO: A method for crystal structure prediction, Comput. Phys. Commun. **183**, 2063 (2012).

[21] X. Shao, J. Lv, P. Liu, S. Shao, P. Gao, H. Liu, Y. Wang, and Y. Ma, A symmetry-orientated divide-and-conquer method for crystal structure prediction, J. Chem. Phys. **156**, 014105 (2022).

[22] See Supplemental Material at http://link.aps.org/supplemental/10.1103/PhysRevB.109.184102 for computational details; convex hull of Na-He-H compounds at 180 GPa obtained from AIRSS; detailed unit-cell parameters and atomic positions of the stable Na-He-H compounds at 180 GPa; crystal structures of stable Na-He-H compounds; crystal structures of stable Na-He-H compounds; crystal structures of metastable *R*-3-Na_3HeH_3 at 180 GPa. It also contains Refs. [7,13,33–36,38,39].

[23] A. Togo, F. Oba, and I. Tanaka, First-principles calculations of the ferroelastic transition between rutile-type and $CaCl_2$-type SiO_2 at high pressures, Phys. Rev. B **78**, 134106 (2008).

[24] W. Kohn and L. J. Sham, Self-consistent equations including exchange and correlation effects, Phys. Rev. **140**, A1133 (1965).

[25] G. Kresse and J. Furthmüller, Efficient iterative schemes for *ab initio* total-energy calculations using a plane-wave basis set, Phys. Rev. B **54**, 11169 (1996).

[26] J. P. Perdew, K. Burke, and M. Ernzerhof, Generalized gradient approximation made simple, Phys. Rev. Lett. **77**, 3865 (1996).

[27] G. Kresse and D. Joubert, From ultrasoft pseudopotentials to the projector augmented-wave method, Phys. Rev. B **59**, 1758 (1999).

[28] H. J. Monkhorst and J. D. Pack, Special points for Brillouin-zone integrations, Phys. Rev. B **13**, 5188 (1976).

[29] P. Giannozzi, O. Andreussi, T. Brumme, O. Bunau, M. B. Nardelli, M. Calandra, R. Car, C. Cavazzoni, D. Ceresoli, and M. Cococcioni, Advanced capabilities for materials modelling with Quantum ESPRESSO, J. Phys.: Condens. Matter **29**, 465901 (2017).

[30] M. Kawamura, FermiSurfer: Fermi-surface viewer providing multiple representation schemes, Comput. Phys. Commun. **239**, 197 (2019).

[31] N. I. Kulikov, McMillan-Hopfield factor and ideal resistivity of transition metals, J. Phys. F: Met. Phys. **8**, L137 (1978).

[32] J. M. McMahon and D. M. Ceperley, Ground-state structures of atomic metallic hydrogen, Phys. Rev. Lett. **106**, 165302 (2011).

[33] L. Monacelli, M. Casula, K. Nakano, S. Sorella, and F. Mauri, Quantum phase diagram of high-pressure hydrogen, Nat. Phys. **19**, 845 (2023).

[34] C. J. Pickard and R. J. Needs, *Ab initio* random structure searching, J. Phys.: Condens. Matter. **23**, 053201 (2011).

[35] P. Baettig and E. Zurek, Pressure-stabilized sodium polyhydrides: NaH_n ($n > 1$), Phys. Rev. Lett. **106**, 237002 (2011).

[36] Y. Hinuma, T. Hatakeyama, Y. Kumagai, L. A. Burton, H. Sato, Y. Muraba, S. Iimura, H. Hiramatsu, I. Tanaka, and H. Hosono, Discovery of earth-abundant nitride semiconductors by computational screening and high-pressure synthesis, Nat. Commun. **7**, 11962 (2016).

[37] S. Wu, X. Yang, H. Zhang, L. Shi, Q. Zhang, Q. Shang, Z. Qi, Y. Xu, J. Zhang, and N. Tang, Unambiguous identification of carbon location on the N site in semi-insulating GaN, Phys. Rev. Lett. **121**, 145505 (2018).

[38] X. Li, X. Zhang, A. Bergara, Y. Liu, and G. Yang, Structural and electronic properties of Na-BH compounds at high pressure, Phys. Rev. B **106**, 174104 (2022).

[39] X. Jiang, Y. Zheng, X. Xue, J. Dai, and Y. Feng, *Ab initio* study of the miscibility for solid hydrogen helium mixtures at high pressure, J. Chem. Phys. **152**, 074701 (2020).

[40] R. F. W. Bader, Atoms in molecules, Acc. Chem. Res. **18**, 9 (1985).

[41] Z. Liu, Q. Zhuang, F. Tian, D. Duan, H. Song, Z. Zhang, F. Li, H. Li, D. Li, and T. Cui, Proposed superconducting electride Li_6C by *sp*-hybridized cage states at moderate pressures, Phys. Rev. Lett. **127**, 157002 (2021).

[42] A. Das, K. Pal, P. Acharyya, S. Das, K. Maji, and K. Biswas, Strong antibonding I(p)–Cu(d) states lead to intrinsically low thermal conductivity in $CuBiI_4$, J. Am. Chem. Soc. **145**, 1349 (2023).

[43] J. J. Zuckerman, Crystal field splitting diagrams, J. Chem. Educ. **42**, 315 (1965).

[44] X. Zhang, Y. Yao, S. Ding, A. Bergara, F. Li, Y. Liu, X. F. Zhou, and G. Yang, Superconductivity in Li_8Au electride, Phys. Rev. B **107**, L100501 (2023).

[45] Z. Zhao, S. Zhang, T. Yu, H. Xu, A. Bergara, and G. Yang, Predicted pressure-induced superconducting transition in electride Li_6P, Phys. Rev. Lett. **122**, 097002 (2019).

[46] J. S. Tse, Y. Yao, and K. Tanaka, Novel superconductivity in metallic SnH_4 under high pressure, Phys. Rev. Lett. **98**, 117004 (2007).

[47] L. Chen, A. Cui, M. Li, S. Li, S. Gong, K. Jiang, J. Zhang, L. Zhu, L. Shang, and Y. Li, Optical excitation-induced ultrafast amorphization in the Y-Sb-Te alloy system: Insights from real-time time-dependent DFT with molecular dynamics calculations, Phys. Rev. B **106**, 214110 (2022).

[48] Y. Ma, A. R. Oganov, and Y. Xie, High-pressure structures of lithium, potassium, and rubidium predicted by an *ab initio* evolutionary algorithm, Phys. Rev. B **78**, 014102 (2008).

[49] Y. Shi and S. Ye, First principles study on electronic structure and optical properties of novel Na-hP4 high pressure phase, Trans. Nonferrous Met. Soc. China **20**, 1092 (2010).

[50] H. Liu, I. I. Naumov, R. Hoffmann, N. W. Ashcroft, and R. J. Hemley, Potential high-T_c superconducting lanthanum and yttrium hydrides at high pressure, Proc. Natl. Acad. Sci. USA **114**, 6990 (2017).